Chiral Shape Engineering Combined with Bimetallic Nanostructures for High-Performance Plasmonic Sulfide Sensors

Han Lin,[ab] *Kuniharu Ijiro,*[b] *Hideyuki Mitomo**[bc]

[a] Graduate School of Life Science, Hokkaido University, Kita 10, Nishi 8, Kita-Ku, Sapporo 060-0810, Japan

[b] Research Institute for Electronic Science, Hokkaido University, Kita 21, Nishi 10, Kita-Ku, Sapporo 001-0021, Japan

[c] Institute of Multidisciplinary Research for Advanced Materials, Tohoku University, Sendai 980-8577, Japan

E-mail: mitomo@es.hokudai.ac.jp

ABSTRACT

Combining chiral shape engineering with the plasmonic sensor features significantly enhances sensor performance and effectively avoids potential background interference. These advantages suggest that chiral nanoparticles could provide valuable insights into addressing defects or shortcomings in traditional plasmonic sensors. Herein, to address the common drawback of performance degradation due to linewidth broadening in plasmonic sulfide sensors during sulfidation, we designed a distinctive intrinsically chiral bimetallic core-shell plasmonic nanoparticle. The chiral gold core provided strong chiroptical activities, enriching the spectral features, including bipolar peaks and zero-crossing points, while the silver shell was used for sulfide sensing. Remarkably, this chiral plasmonic sulfide sensor demonstrated exceptional sensitivity and clarity. Specifically, the zero-crossing point in the circular dichroism spectrum serves as an easily recognizable tracking feature, leveraging the trend of linewidth broadening to enhance sensor responsiveness. Particularly, at a sulfide concentration of only 5 μM, the zero-crossing point shift reached up to 170 nm, with a maximum shift limit of 208 nm, surpassing all previously reported plasmonic sulfide sensors. Finally, the well-defined structure of this chiral-core sensing-shell design offers an alternative fabrication approach for expanding the chiral plasmonic sensing platform, allowing for flexible replacement of the shell material to meet specific sensing requirements.

INTRODUCTION

Sensitive and selective detection of sulfides (particularly sulfide ions and hydrogen sulfide) is of significant importance for environmental protection, public health maintenance, and the prevention and treatment of diseases.[1–3] Plasmonic metal nanoparticles have emerged as strong candidates for the development of next-generation sulfide sensors due to their ability to achieve specific binding to sulfides, real-time response, and visual diagnosis.[4–6] Additionally, these particles offer potential solutions for endogenous sulfides, including bioimaging, drug delivery, and targeted therapy.[7–9] These advantages are primarily attributed to the localized surface plasmon resonance (LSPR) effect of plasmonic nanoparticles, the optical properties of which are highly dependent on particle shape, composition, and the surrounding dielectric environment.[10–14] Therefore, the rational design of plasmonic nanoparticles will directly enhance the performance of the sensors.[15–17]

Gold-silver (Au-Ag) core-shell nanoparticles are a classic structure in the construction of plasmonic sulfide sensors.[18] In the presence of oxygen, the Ag shell is selectively etched by sulfides to form Ag_2S, causing significant changes in the dielectric environment around the Au core and leading to LSPR peak shifts. Based on this sensing mechanism, the responsiveness of the LSPR peak position has been regarded as a primary indicator of plasmonic sensor sensitivity.[19] Notably, this responsiveness is reflected not only in the sensor's acute reaction to subtle environmental changes but also in the broad range of the peak shift ($\Delta\lambda$). Typically, a narrower plasmonic linewidth (as indicated by the full width at half maximum, FWHM) favors improved sensitivity, as a wider FWHM can mask peak position changes due to peak broadening.[20] In pursuit of this, various Au core shapes, including spheres, dimers, rods, cubes, triangular plates, rhombic dodecahedra, and bipyramids, have been widely explored.[18,21–26] However, due to the inherent

limitation of high ohmic losses in metallic materials, the FWHM of Au nanostructures is difficult to reduce below 80 nm.[27] Furthermore, the FWHM of traditional Au@Ag core-shell structures significantly broadens with increasing sulfuration, primarily due to the plasmon damping effect intensified by silver sulfide (Ag_2S) as a semiconductor material, which further weakens sensor sensitivity and detection accuracy.[28,29] Consequently, developing a more robust and efficient structural design to overcome these inherent limitations remains a critical task for advancing high-performance plasmonic sulfide sensors.

Incorporating chiral shape factors into the design of plasmonic nanoparticles holds great promise for significantly enhancing sensor sensitivity, as circular dichroism (CD) spectra offer additional, more distinct features for tracking, such as dipolar peaks and zero-crossing points.[30] The zero-crossing point indicates that the chiral nanoparticles exhibit equal absorption intensities for left- and right-handed circularly polarized light at this wavelength.[31,32] An impressive example of this is the femtomolar-level protein sensing achieved using chiral nanospiral metamaterials, highlighting the potential of chiral plasmonic sensors to overcome the limitations of traditional plasmonic sulfide sensors.[33] In particular, compared to detecting higher concentrations of sulfides in the environment, such as the wastewater from mining, petroleum refining, and paper industry, sensitively and accurately detecting lower concentrations of sulfides poses a formidable and urgent challenge. For instance, hydrogen sulfide within biological systems has been shown to be associated with various pathological and physiological processes,[34] and accurate detection of its concentration is beneficial for medical research and clinical diagnosis.[35] Additionally, detecting sulfides in groundwater can aid in environmental quality assessment and ecosystem protection.[36] However, plasmonic metamaterials with high chiral shape factors or strong chiroptical activities were typically fabricated through top-down strategies.[37–40] The high cost, limited yield, and

restricted variety of such structures pose significant challenges to the broader adoption of chiral plasmonic sensors as next-generation sensing platforms.

In recent years, significant progress has been made in the synthesis of intrinsic chiral plasmonic nanoparticles via wet chemical methods.[41–44] However, research remains predominantly focused on pure Au materials, with limited reports on chiral nanoparticles of Ag, other metals, or even alloys.[45] This scarcity may stem from differences in the reduction kinetics between metals and the binding affinities of involved ligands. As a promising alternative, the use of chiral gold nanoparticles as cores to create bimetallic core-shell structures offers great potential for advancing chiral plasmonic sensors. Herein, we present a high-performance sulfide sensor based on intrinsic chiral Au core-sensing Ag shell plasmonic nanoparticles (c-Au@Ag NPs, Scheme 1A). Traditional plasmonic sensing, which interprets signals through LSPR peak shifts ($\Delta\lambda_{LSPR}$), often faces limitations in sensitivity and resolution due to line broadening (Scheme 1B). In contrast, CD-based sensing strategies offer more distinct and recognizable response features. Specifically, shifts in the zero-crossing point ($\Delta\lambda_0$) of the CD spectra can provide a broader range of response shifts than CD peak shifts ($\Delta\lambda_m$) due to changes in line broadening trends (Scheme 1C). Additionally, in the lower sulfide concentration range (0.1-5 μM), this chiral plasmonic sensor demonstrated a robust linear response relationship, with $\Delta\lambda_0$ consistently maintaining the highest sensitivity (Scheme 1D). Finally, this sensor demonstrated exceptional selectivity for sulfide ions when challenged with numerous common interfering ions.

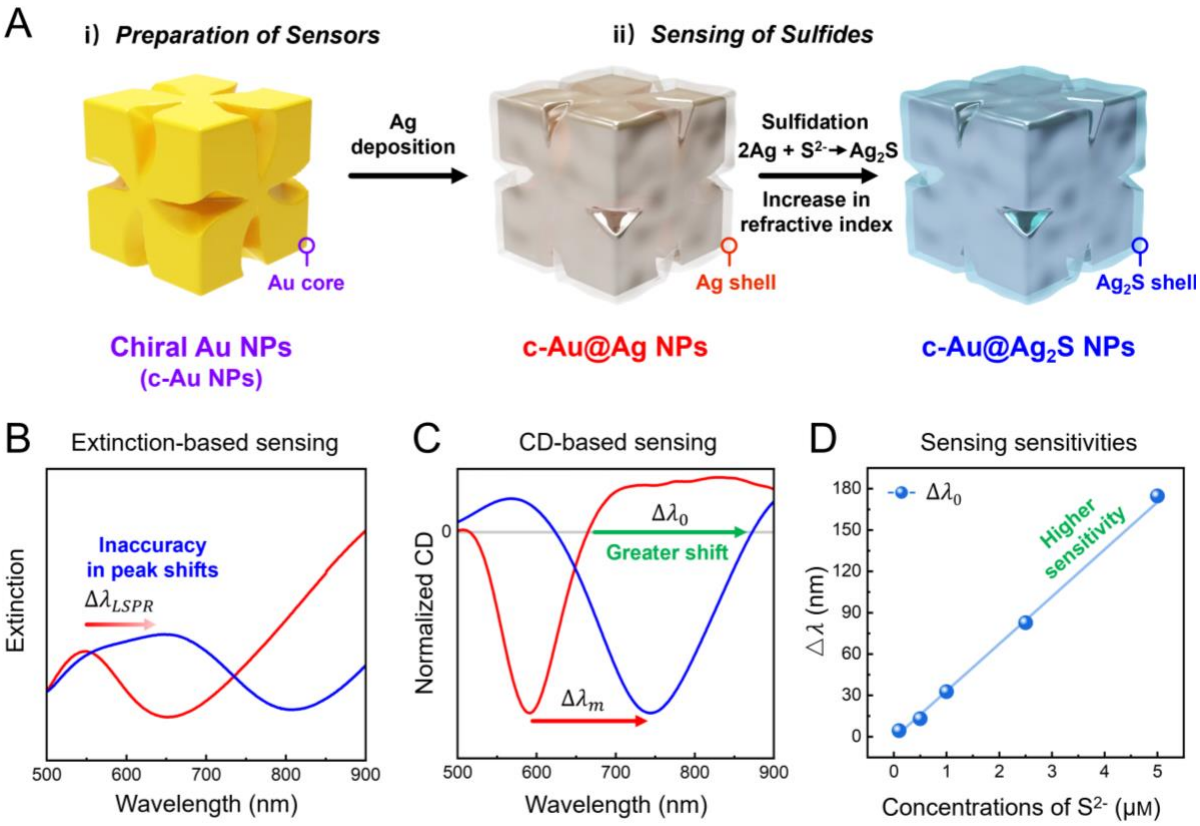

Scheme 1. A sulfide-sensing platform based on chiral Au core-Ag shell plasmonic nanoparticles (c-Au@Ag NPs). (A) Schematic illustration of the preparation and sensing mechanism of c-Au@Ag NPs. During the sulfide sensing process, changes were observed in (B) the extinction and (C) CD spectra. (D) The relationship of peak shifts in the zero-crossing point ($\Delta\lambda_0$) with sulfide concentration.

RESULTS and DISCUSSION

Morphology, Composition and Optical Response of the c-Au@Ag NPs

First, c-Au NPs were synthesized by using Au octahedral particles (Au ONPs) as seeds through a regrowth method (Figure S1, S2),[41] exhibiting significant chiroptical activities around 615 nm (g-factor $= -0.028$). Subsequently, the c-Au@Ag NPs core-shell structures were prepared via Ag layer coating on the surface of the c-Au NPs by epitaxial growth method (Figure 1A).[46] Despite the surface chiral characteristics of the c-Au NPs were revealed to consist of a windmill-like structure formed by twisted arms and internal gaps connected by fourfold rotational symmetry, energy-dispersive X-ray spectroscopy (EDS) images of c-Au@Ag NPs (Figure 1B and Figure S3) showed that Ag atoms almost completely covered the Au surface, and clear Ag lattice fringes were observed in high-resolution transmission electron microscopy (HRTEM) images (Figure S4). This was attributed to the minimal lattice constant difference of only 0.2% between Ag and Au, causing Ag atom deposition to mainly follow a layer-by-layer growth mode (Frank–van der Merwe mode).[46] The presence of diffraction spots in the diffraction image (Figure S5) further supports this perspective, as opposed to the diffraction rings that would be expected in a non-epitaxial growth mode. However, compared to the protruding arms, the recessed gaps were more likely to form preferred deposition sites for Ag atoms (Figure 1C). Particularly, as the Ag concentration in the growth environment increased (from i to iv), this preferential deposition became more pronounced, resulting in the filling of internal gaps. This preferential deposition could be a beneficial way to reduce the overall surface energy of the particles, a similar phenomenon observed in the coating of Au nanostars (possessing both concave and convex surfaces) with Ag layers.[47,48] From an optical response perspective, as the Ag content in the bimetallic composition increased, the color of the colloidal solution transitioned from purple to red and even to orange (Figure S6).

Correspondingly, the LSPR peak (λ_{LSPR}) located near 570 nm gradually blue shifted (Figure 1D). This change caused the nearby CD bands to which this resonance mode contributes, including the peak position (λ_m) and zero-crossing point (λ_0), to also blue shift, accompanied by a decrease in peak intensity (Figure 1E, F). The reduction in peak intensity was likely due to the introduction of Ag as an achiral component or changes in particle morphology, which reduced their inherent chiral characteristics. This phenomenon was also corroborated by the corresponding *g*-factor spectra (Figure S7). In our previous reports, we also observed a phenomenon by which the chiroptical activities of the chiral nanoparticles were diminished due to modification with an achiral coating.[49]

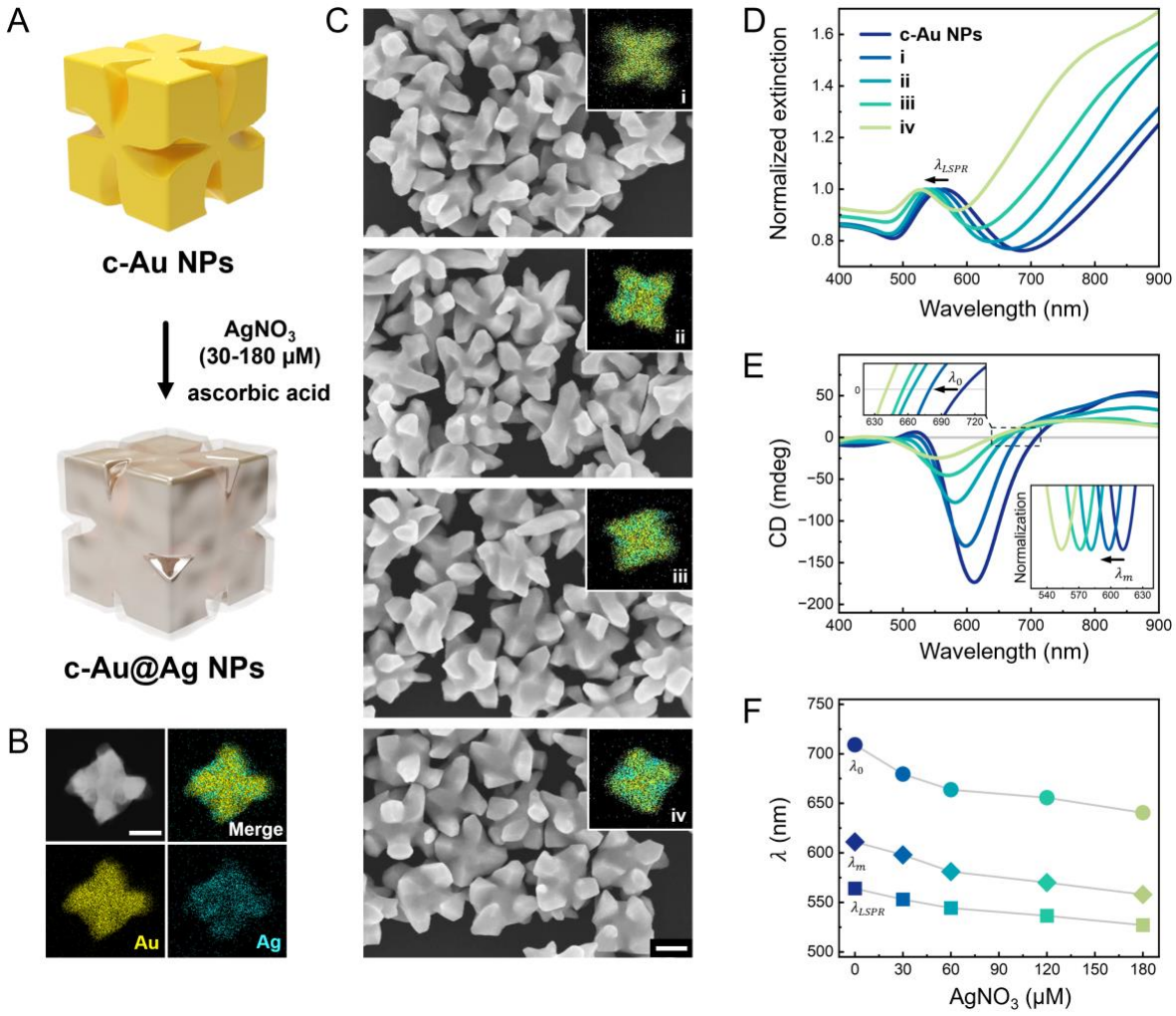

Figure 1. Characterization of c-Au@Ag NPs. (A) Schematic illustration of c-Au@Ag NPs prepared via the epitaxial growth method. (B) HAADF-STEM image and corresponding EDS mapping images of c-Au@Ag NPs (ii). (C) SEM images and EDS mapping images (the insets) of c-Au@Ag NPs with varying Ag content (from i to iv, the final concentrations of Ag were 30, 60, 120, and 180 μM, respectively). (D) Normalized extinction spectra and (E) CD spectra of c-Au NPs and c-Au@Ag NPs with different Ag content. (F) Shift variations of λ_{LSPR}, λ_m, and λ_0 after the addition of different amounts of silver nitrate ($AgNO_3$). The scale bars are 100 nm.

Optimization of the Ag Content in c-Au@Ag NPs

As the common evaluation criteria for sensors, sensitivity is one of the crucial metrics that must be considered.[50] It is typically quantified as the ratio of the peak shift ($\Delta\lambda$) in the plasmonic nanoparticle resonance wavelength to the corresponding change in the refractive index (Δn) of the surrounding environment, as shown in equation (1):

$$\mathrm{Sn} = \frac{\Delta\lambda}{\Delta n} \qquad (1)$$

In other words, sensitivity can be indirectly evaluated by measuring the peak shift that occurs before and after complete sulfidation of the particle, as the corresponding change in refractive index remains largely similar.[51] Moreover, the value of $\Delta\lambda$ can be maximized by adjusting the Ag content in the bimetallic structure. To achieve this, the experiment was conducted in a relatively high concentration (25 μM) of sulfide ions to ensure the complete sulfidation of the nanoparticles with varying Ag content (Figure 2A). The EDS results also supported the occurrence of the sulfidation reaction, though it is important to note the potential for misleading information in the mapping images due to false sulfur signals. This phenomenon arose from the close proximity of the characteristic X-ray peaks of Au and sulfur (Figure S8), which may have caused portions of the Au signal to be incorrectly attributed to sulfur. Consequently, even unsulfidized particles could exhibit sulfur-like distributions on their surfaces (Figure S9). To avoid this potential interference, we verified the sulfidation reaction by focusing exclusively on characteristic protrusions at the particle edges, confirming that these protrusions were composed of Ag_2S (Figure 2B). Notably, as the silver content in the particles increased, the protrusions became more pronounced (Figure 2C).[24] The corresponding extinction spectra exhibited broad LSPR peaks, particularly at the highest Ag content, making it difficult to distinguish the peak shifts before and after sulfidation (Figure 2D). The dynamic light scattering (DLS) results (Figure S10) ruled out the possibility that

nanoparticle aggregation during the sulfuration process affected the spectral response. The broad peaks were likely due to the multiple Ag_2S protrusions through resonance coupling with the particle surface. It was noteworthy that the CD and *g*-factor spectra provided more intuitive peak shape changes (Figure 2E and Figure S11), possibly because the Ag_2S layer had extinction activities but lacked chiroptical activities. After the sulfidation, the λ_m and λ_0 of the first three groups (i, ii, and iii) of c-Au@Ag NPs all showed a red shift trend. Unfortunately, the λ_0 of the third group (iii) could not be recorded due to the instrument limitation on detectable range of wavelength. However, the CD peak shape remained clearly discernible, indicating that c-Au@Ag NPs (iii) had the potential for higher sensitivity. We predicted that its sensing performance could be better captured and assessed with more advanced detectors, such as near-infrared detectors. In contrast, the fourth group (iv) exhibited broad peaks with weak intensity, making it difficult to pinpoint specific λ_m and λ_0 values. It should be noted that this phenomenon was more attributable to the reduced detection limit of the sensor itself rather than instrumental limitations. This indicated that Ag affected the performance of chiral plasmonic sulfide sensors in two ways. Firstly, Ag conferred the ability to sense sulfides, and its content directly affected the sensitivity (Figure S12). Secondly, Ag caused a loss in overall chiral characteristics and intensity, leading to a significant decrease in detection accuracy and data reliability. Based on these considerations, the ideal situation would be to use less Ag as the sensing layer to achieve better sensor performance. As shown in the Figures 2F and S13, the second group (ii) of c-Au@Ag NPs exhibited higher sensitivity, with a shift of up to 208 nm by $\Delta\lambda_0$ before and after sulfidation. Therefore, this c-Au@Ag NPs was selected for further research as a chiral plasmonic sulfide sensor.

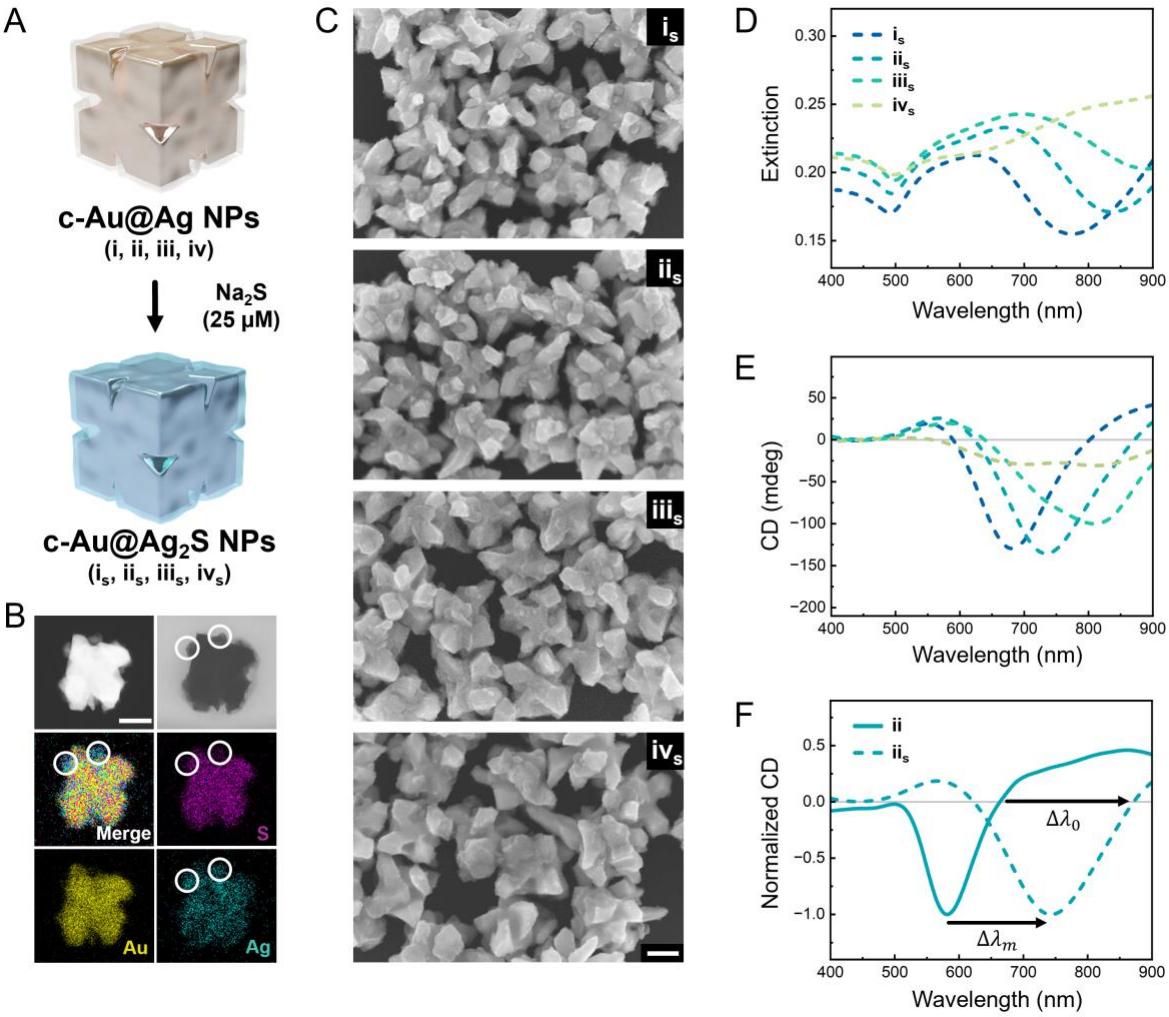

184

185 **Figure 2.** Characterization of c-Au@Ag_2S NPs. (A) Schematic illustration of c-Au@Ag_2S NPs
186 obtained after sulfidation from c-Au@Ag NPs (final sulfide ion concentration: 25 μM). (B) STEM
187 image, HAADF-STEM image and corresponding EDS mapping images of c-Au@Ag_2S NPs (ii_s).
188 The typical Ag_2S protrusions were shown within the white circles. (C) SEM images of c-
189 Au@Ag_2S NPs (i_s, ii_s, iii_s and iv_s) obtained after sulfidation from c-Au@Ag NPs (i, ii, iii and iv).
190 (D) Extinction spectra and (E) CD spectra of c-Au@Ag_2S NPs (i_s, ii_s, iii_s and iv_s). (F) Normalized
191 CD spectra of c-Au@Ag NPs before (ii) and after (ii_s) sulfuration. The scale bars are 100 nm.

Chiroptical Sensing of Sulfides using c-Au@Ag NPs

The chiroptical sensing of sulfides by c-Au@Ag NPs was closely related to the conversion of the Ag layer on the particle surface into Ag_2S (Figure 3A). To investigate this process in detail, digital photographs were recorded of c-Au@Ag NPs after incubation in different sulfide ion concentrations (0-25 μM), along with their corresponding extinction and *g*-factor spectra. As the sulfide ion concentration gradually increased, the color of the colloidal solution gradually transitioned from pink to blue (Figure 3B). The extinction spectra revealed a red shift of approximately 24 nm in the λ_{LSPR} when the sulfide ion concentration reached 5 μM, accompanied by a notable increase in FWHM (Figure 3C, D). Further increases in the sulfide ion concentration to 10 μM and 25 μM resulted in the emergence of an additional LSPR peak (will be explained in the subsequent section) at a higher wavelength range (650-700 nm), which coupled with the original LSPR peak to form a broad peak, making it difficult to accurately discern the λ_{LSPR} shift. In contrast, the CD spectra did not exhibit such peak shifts. The normalized spectra clearly demonstrated a red shift in λ_m with increasing sulfide ion concentration (Figure 3E). When the concentration of sulfide ion increased from 10 μM to 25 μM, the red shift slowed significantly, ultimately reaching 148 nm (Figure 3F). During the sulfidation process, the FWHM of the characteristic peaks inevitably increased, which is generally considered disadvantageous. However, the λ_0 in CD spectra could leverage this trend, exhibiting a more significant redshift, reaching up to 208 nm (Figure 3G, H). Compared to sensors suitable for detecting high and wide ranges of sulfide ion concentrations (hundreds of μM), this chiral plasmonic sensor exhibited significant shift capabilities within a relatively low and narrow sulfide concentration range (0.1-5 μM). This indicated its potential to capture changes in sulfide concentration in specific

environments, such as the minor fluctuations in sulfide levels in the body caused by cellular anabolic and catabolic processes.[52]

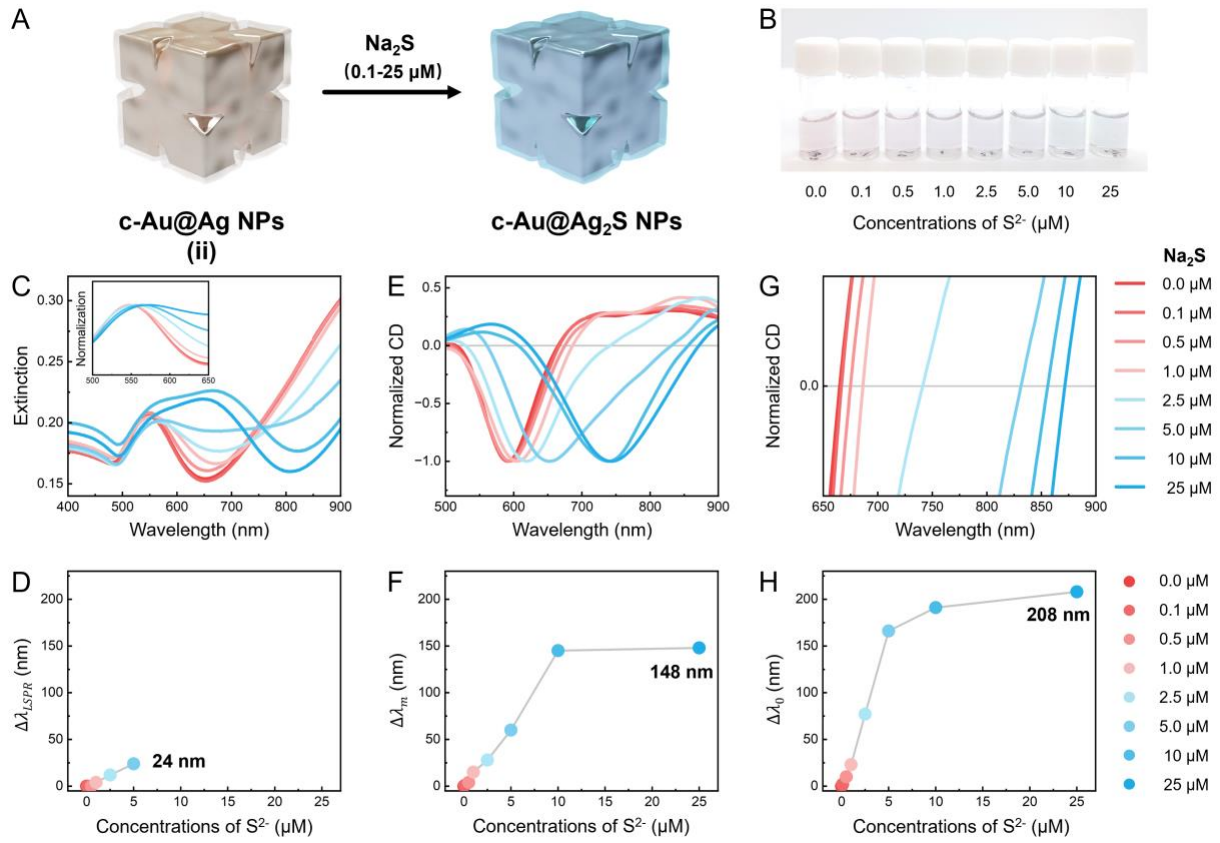

Figure 3. Optical response of the chiral plasmonic sulfide sensor. (A) Schematic illustration of c-Au@Ag NPs for sulfide sensing. (B) The digital photograph of c-Au@Ag NPs colloidal solutions under a range of sulfide ion concentrations. (C) Extinction spectra and the magnified normalized extinction spectra (inset) of c-Au@Ag NPs at different sulfide ion concentrations, along with (D) the associated shifts in λ_{LSPR}. (E) Normalized CD spectra of c-Au@Ag NPs at different sulfide ion concentrations, and (F) the corresponding shifts in λ_m. (G) The magnified normalized CD spectra of c-Au@Ag NPs at different sulfide ion concentrations, and (H) the corresponding shifts in λ_0.

To better understand the observed optical response behaviors, SEM images were obtained to document the morphological changes in c-Au@Ag NPs following incubation in varying concentrations of sulfide ions. When the sulfide ion concentration was increased from 0.1 to 1 μM (Figure 4A and Figure S14), the particle morphology remained largely unchanged, indicating that the reaction at this stage was primarily dominated by a uniform outward-to-inward sulfidation process. However, as the sulfide ion concentration increased to 2.5 μM (Figure 4B), one or two small Ag_2S protrusions began to appear randomly within the recessed gaps on the particle surface. With a further increase in sulfide ion concentration to 5 μM (Figure 4C), both the number and size of these protrusions increased, yet they remained primarily located in the recessed areas. These protrusions may have formed because the recessed areas are rich in Ag content and exhibit higher surface energies, providing more favorable nucleation sites that consume excess sulfide ions during the initial stages of the reaction, until the sulfidation rate equilibrates with the diffusion rate.[24] When the sulfide ion concentration was further increased to 10 μM (Figure 4D), the anisotropic sulfidation differences diminished, with smaller protrusions appearing randomly across other areas in addition to the larger ones in the recessed regions. At this period, the characteristic peaks no longer exhibited significant red shifts, suggesting that either the particles had nearly completed sulfidation or the refractive index had ceased to increase. Furthermore, it is worth noting that the high density of surface protrusions led to significant changes in the overall morphology and roughness of the particles, which might have induced multiple resonance mode coupling, thereby contributing to the broad peaks observed in the extinction spectra.[53]

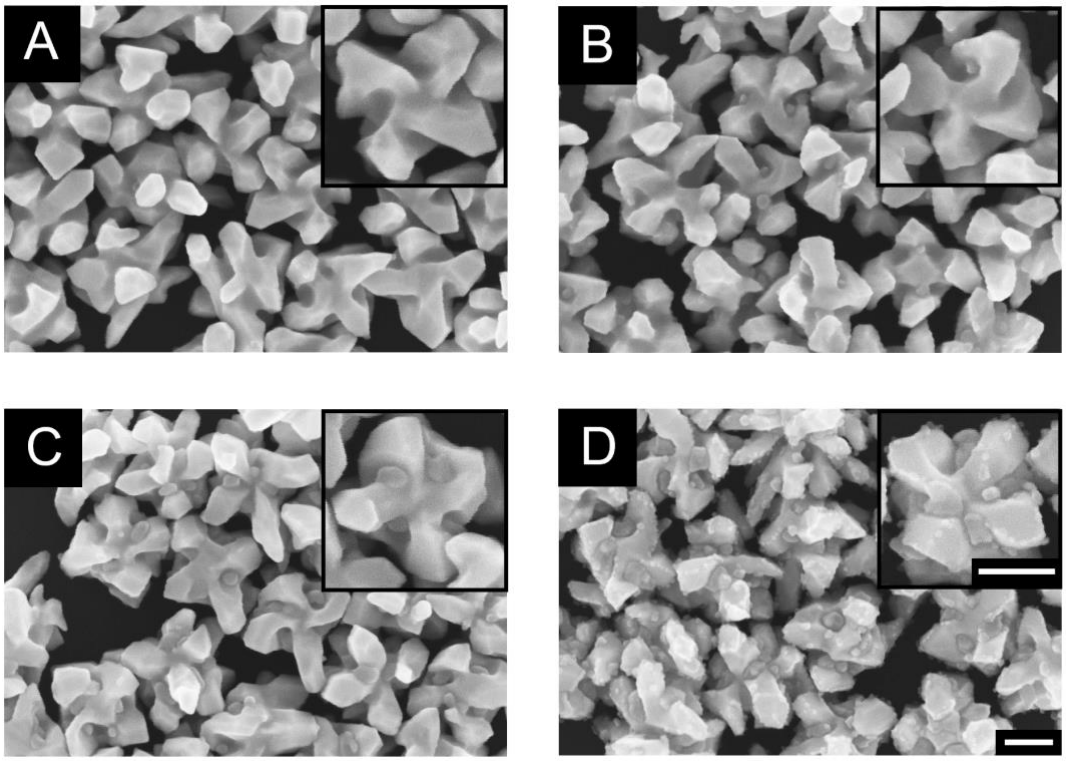

245

246 **Figure 4.** Morphological changes in c-Au@Ag_2S NPs after incubation with varying sulfide ion
247 concentrations. SEM images of c-Au@Ag_2S NPs after incubation with sulfide ion concentrations
248 of 1 μM (A), 2.5 μM (B), 5 μM (C), and 10 μM (D). The scale bars are 100 nm.

Performance Evaluation of c-Au@Ag NPs as a Chiral Plasmonic Sulfide Sensor

To validate the feasibility of c-Au@Ag NPs as a chiral plasmonic sensor for sulfide detection, a comprehensive evaluation of its sensing performance is necessary. In this study, we focused on the precise detection of sulfide ions in aqueous solutions. Initially, when c-Au@Ag NPs were exposed to a sulfide ion environment (2.5 μM), the CD peak exhibited a red shift and intensity decrease within 5 min (Figure S15). Extending the reaction time further had not significant affect on the spectral changes, indicating that the sulfuration process was complete. Subsequently, we recorded the peak shifts of various spectra at different sulfide ion concentrations (Figure 5A). Even in lower concentrations of sulfide ions, this detection strategy provided a clear linear curve. This suggests that under the current experimental conditions, the diffusion of sulfide ions did not limit the reaction rate. However, if the solution to be tested is a viscous fluid (such as body fluid), the detection time may need to be appropriately extended to ensure the reaction is fully completed. Compared to the changes in the extinction spectra ($\Delta\lambda_{LSPR}$), the red shifts of the characteristic peaks in the CD spectra ($\Delta\lambda_m$ and $\Delta\lambda_0$) demonstrated good linear relationships over a wider range of sulfide ion concentrations (0.1-5 μM), with $\Delta\lambda_0$ exhibited the most significant shift and the highest linear correlation coefficient ($R^2 = 0.996$). Cross-validation based on multi-channel sensing signal output can effectively reduce the occurrence of false negatives or positives (Figure S16),[54] resembling dual-signal sensing strategies that enhance detection reliability by analyzing both peak shifts and extinction intensity changes in extinction spectra.[55] By comparing the slopes of the linear equations ($\Delta\lambda/S^{2-}$), the relative sensitivities of the three characteristic peak shifts were evaluated. For instance, the sensitivity of $\Delta\lambda_0$ was approximately three times larger than that of $\Delta\lambda_m$ and six times larger than that of $\Delta\lambda_{LSPR}$, lowering the limit of detection (LoD) to 0.1 μM. This performance significantly surpassed previously reported fluorescence-based organic molecular

probes for sulfide detection in live cells, whose LoD ranged from 1 to 10 μM, achieving an improvement of 1 to 2 orders of magnitude.[56-58] Furthermore, upon complete sulfuration of the c-Au@Ag NPs, λ_0 achieved a maximum red shift of 208 nm, surpassing the sensing limits reported for other plasmonic sulfide sensors (Figure 5B). Selectivity is also an important criterion for evaluating sensor performance. As shown in the Figure S17, the normalized CD spectra were recorded after incubating c-Au@Ag NPs in the presence of sulfide ions, a series of interfering ions (at 10 times higher concentration than that of sulfide ions), and their mixtures. Only the sulfide ions and their mixed solutions induced significant and similar shift changes (Figure 5C and Figure S18). Moreover, the corresponding colloidal solution turned blue, whereas the other interfering ions did not cause noticeable color changes (Figure S19). These results indicated that c-Au@Ag NPs exhibited high selectivity for sulfide detection, likely due to the extremely low solubility product constant of Ag_2S ($K_{SP} = 6.3\times10^{-50}$).[59]

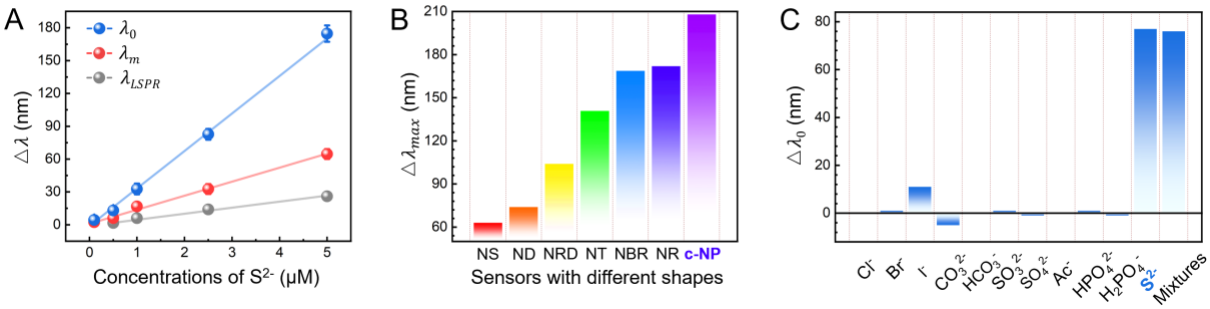

Figure 5. Performance of c-Au@Ag NPs as a chiral plasmonic sulfide sensor. (A) Linear relationships between peak shifts in the extinction spectra ($\Delta\lambda_{LSPR}$: gray, $y = 4.989x - 0.900$, $R^2 = 0.991$) and CD spectra ($\Delta\lambda_m$: red, $y = 11.936x - 0.103$, $R^2 = 0.994$; $\Delta\lambda_0$: blue, $y = 33.625x - 4.665$, $R^2 = 0.996$) with varying sulfide ion concentrations. (B) Comparison of the maximum shift ($\Delta\lambda_{max}$) of c-Au@Ag NPs with other plasmonic sulfide sensors. Other sensors all featured Au-core-Ag shell structures with varying core shapes, including nanospheres (NS),[18] nano

291 dimers (ND),[21] nanorods (NR),[22] nano triangular plates (NTP),[24] nano rhombic dodecahedras
292 (NRD),[25] and nano bipyramids (NBR).[26] (C) The zero-crossing point shifts ($\Delta\lambda_0$) of c-Au@Ag
293 NPs after incubation in the presence of sulfide ions (2.5 μM), other interfering ions (25 μM) and
294 their mixtures (sulfide ions at 2.5 μM and all the aforementioned interfering ions at 25 μM).

CONCLUSIONS

In summary, we have demonstrated a distinctive chiral bimetallic core-shell nanoparticle as a chiral plasmonic sensor for efficient sulfide detection. Unlike traditional plasmonic sulfide sensors, this chiral sensor provided clearer characteristic signals for tracking in its CD spectrum. Notably, the zero-crossing point in the CD spectrum was not only easy to identify but also effectively leveraged the trend of increasing linewidth, significantly enhancing the sensor's sensitivity. Furthermore, previous studies had indicated that the intrinsic chiral characteristics of chiral plasmonic nanoparticles could promote interactions with biological systems, such as reducing protein corona formation and enhancing cellular uptake efficiency.[60] This potential advantage positions the chiral plasmonic sensor favorably for the efficient detection of endogenous sulfides *in vivo*. Future research will focus on integrating machine learning algorithms and multi-signal cooperative detection strategies to overcome current instrumentation limitations,[61] further enhancing detection capabilities, including reliability and measurable range, a direction our research group is actively pursuing. Last but not least, the proposed structural design of the chiral core-sensor shell provides a promising reference scheme for customizing chiral plasmonic sensing platforms, allowing for the flexible adjustment of shell materials based on analyte requirements, including responsive molecules, polymers, and metals.

METHODS

Materials. Chloroauric acid ($HAuCl_4 \cdot 3H_2O$, 99.9%), L-Glutathione reduced (L-Gsh, ≥98.0%), sodium borohydride ($NaBH_4$, 99.0%), ascorbic acid (AA, 99%), cetrimonium bromide (CTAB, BioXtra, ≥99%), potassium iodide (KI, ≥99.0%) and sodium iodide (NaI, ≥99.5%) were purchased

317 from Sigma-Aldrich. Hexadecyltrimethylammonium chloride (CTAC) and silver nitrate ($AgNO_3$,
318 99.8%) were purchased from FUJIFILM Wako Pure Chemical Corp. (Osaka, Japan).
319 **Characterization.** The UV-vis and CD spectra of the sample aqueous solutions were recorded
320 using a JASCO V-770 spectrophotometer and J-1500 spectropolarimeter, respectively. The path
321 length of the cuvette was 1 cm. The CD measurements were conducted with the following
322 parameter settings: a scan speed of 200 nm/min, a response time of 1 ms, a sampling interval of 1
323 nm, a bandwidth of 10 nm, and two scan repetitions. Field-emission scanning electron microscopy
324 (SEM) measurements were carried out using an ultimate field emission scanning electron SU-8230
325 (Hitachi High-Tech, Tokyo, Japan) at an acceleration voltage of 8 kV. Scanning transmission
326 electron microscope (STEM) observations were carried out using a HD-2000 (Hitachi High-Tech,
327 Tokyo, Japan) with a 200 kV accelerating voltage. High-resolution transmission electron
328 microscopy (HRTEM) images were obtained using a JEM-ARM200F (JEOL Ltd., Tokyo, Japan)
329 with a 200 kV accelerating voltage. The dynamic light scattering (DLS) measurements were
330 performed with a Zetasizer Nano ZS (Malvern Panalytical Ltd, UK).
331 **Synthesis of Au ONPs.** The synthesis of Au ONPs (edge length: 50 nm) was achieved via a
332 seed-mediated method with iodide assistance. First, Au nanoseeds were prepared by rapidly
333 injecting freshly prepared $NaBH_4$ solution (225 μL, 20 mM) into an aqueous CTAC solution (0.1
334 M, 5 mL) containing $HAuCl_4$ (0.25 μM) with vigorous stirring for 2 min. The seed solution was
335 then allowed to age at 30 °C for 1 h to ensure the degradation of excess $NaBH_4$ before use. Next,
336 growth solutions A and B were prepared. Growth solution A consisted of CTAC (5 mL, 0.2 M),
337 water (4.5 mL), $HAuCl_4$ (250 μL, 10 mM), KI (5 μL, 1 mM), and AA (220 μL, 40 mM). Growth
338 solution B consisted of CTAC (40 mL, 0.2 M), water (36 mL), $HAuCl_4$ (2 μL, 10 mM), KI (40 μL,
339 1 mM), and AA (1.76 mL, 40 mM). The seed solution (25 μL) was injected into growth solution

A and shaken for 5 s (the solution turned pale pink). Then, this mixture (200 μL) was quickly transferred to growth solution B, thoroughly mixed, and left to stand at 30 °C for 15 min to allow for particle growth. The products were centrifuged twice (4230*g*, 10 min) to remove excess surfactant, and the collected product was subsequently redispersed in a CTAB solution (1 mM). Prior to the subsequent chiral growth, the final volume of the Au ONPs solution was adjusted such that, after dilution by a factor of 20, the absorbance at a wavelength of 400 nm reached 0.3.

Synthesis of c-Au NPs. The preparation of c-Au NPs was achieved through the regrowth of Au ONPs mediated by chiral ligands L-Gsh. In a typical growth protocol, a growth solution consisting of water (3.458 mL), $HAuCl_4$ (200 μL, 10 mM), CTAB (800 μL, 100 mM), and AA (480 μL, 100 mM) was prepared in a scintillation vial. Subsequently, L-Gsh (27 μL, 2 mM) and Au ONPs (35 μL) were sequentially added to the growth solution, followed by thorough vortexing for 30 s. The mixture was then allowed to stand at a constant temperature in a water bath (30 °C, 2 h) to obtain c-Au NPs. Similarly, the resulting products were centrifuged twice (1440*g*, 6 min), and the collected products were redispersed in a CTAC solution (1 mM).

Synthesis of c-Au@Ag NPs. The c-Au@Ag NPs core-shell structure was achieved through the epitaxial growth of a Ag layer on the Au surface. Specifically, a mixture of CTAC (1.5 mL, 80 mM) and c-Au NPs (75 μL) was prepared in a scintillation vial and preheated in an incubator (65 °C, 10 min). Subsequently, $AgNO_3$ (10 mM) and AA (15 μL, 100 mM) were sequentially added to the above solution, followed by thorough vortexing for 30 s. The vial was then returned to the incubator (65 °C, 4 h). The amount of $AgNO_3$ (5/10/20/30 μL) was varied to adjust the Ag content in the bimetallic composition. The resulting solution was centrifuged twice (1440*g*, 6 min) and redispersed in deionized water, with the final volume maintained at 990 μL.

Detection of sulfide in aqueous solutions. The above c-Au@Ag NPs solution (990 μL) was mixed by vortexing with varying concentrations of Na_2S solution (10 μL), and adjusting the final concentration of sulfide ions to 0.1/0.5/1/2.5/5/10/25 μM. To ensure complete reaction, the samples were allowed to stand at room temperature for 30 min before testing.

Calculation of the *g*-factor. The asymmetry factor of polarization rotation, also known as the *g*-factor, is a concentration-independent parameter. The ratio of the different extinction values of a substance between LCP and RCP light to the total extinction value is calculated using the following formula:

$$g\text{-factor} = \frac{CD(mdeg)}{32980 \cdot \text{Extinction}}$$

ASSOCIATED CONTENT

Supporting Information

The Supporting Information is available free of charge at

Characterization of Au ONPs and c-Au NPs; digital photographs and CD spectra of c-Au NPs and c-Au@Ag NPs; elemental analysis and HRTEM images of c-Au@Ag NPs; DLS characterization of c-Au@Ag_2S NPs; characterization of c-Au NPs before and after incubation in sulfide ions environment; effect of Ag content on the sensing ability of c-Au@Ag NPs; SEM images of c-Au@Ag_2S NPs obtained after incubation in different sulfide ions concentrations; linear correlation between $\Delta\lambda_m$ and $\Delta\lambda_0$ and the characterization of the ability of c-Au@Ag NPs to resist other interfering ions.

AUTHOR INFORMATION

Corresponding Author

*Email: mitomo@es.hokudai.ac.jp (H. Mitomo)

Author Contributions

H. L. and H. M. conceptualized and designed this research. H. L. conducted all experiments and data visualization. K. I. and H.M. supervised the project. The manuscript was written with contributions from all authors. All authors have approved the final version of the manuscript.

Notes

The authors declare no competing financial interests.

ACKNOWLEDGMENT

H. L. acknowledges the financial support (202008330307) from the China Scholarship Council (CSC) for his doctoral studies at Hokkaido University. H. M. is thankful for financial aid from JSPS KAKENHI (Grant no. JP21H01736, and JP24K01275). K. I. is thankful for financial aid from JSPS KAKENHI (Grant no. JP24K03258). K. I. acknowledges support from the "Photoexcitonix Project" and the "Project of Young Investigator Promotion" at Hokkaido University. This work was also supported by the "Crossover Alliance to Create the Future with People, Intelligence and Materials" from the Ministry of Education, Culture, Sports, Science, and Technology of Japan (MEXT). We thank Instrumental Analysis Support Office, the Frontier Chemistry Center, Faculty of Engineering, Hokkaido University for allowing us to conduct CD measurements. A part of this work was supported by "Advanced Research Infrastructure for Materials and Nanotechnology in Japan (ARIM)" of the Ministry of Education, Culture, Sports, Science and Technology (MEXT): Grant Number JPMXP1223HK0051 and JPMXP1224HK0048 (Hokkaido University).

405 REFERENCES

406 (1) Zhang, L.; De Schryver, P.; De Gusseme, B.; De Muynck, W.; Boon, N.; Verstraete, W.
407 Chemical and Biological Technologies for Hydrogen Sulfide Emission Control in Sewer Systems:
408 A Review. *Water Res.* **2008**, *42* (1-2), 1–12.

409 (2) Adgate, J. L.; Goldstein, B. D.; McKenzie, L. M. Potential Public Health Hazards,
410 Exposures and Health Effects from Unconventional Natural Gas Development. *Environ. Sci.*
411 *Technol.* **2014**, *48* (15), 8307–8320.

412 (3) Polhemus, D. J.; Lefer, D. J. Emergence of Hydrogen Sulfide as an Endogenous Gaseous
413 Signaling Molecule in Cardiovascular Disease. *Circ. Res.* **2014**, *114* (4), 730–737.

414 (4) Pensa, E.; Cortés, E.; Corthey, G.; Carro, P.; Vericat, C.; Fonticelli, M. H.; Benítez, G.;
415 Rubert, A. A.; Salvarezza, R. C. The Chemistry of the Sulfur-Gold Interface: In Search of a Unified
416 Model. *Acc. Chem. Res.* **2012**, *45* (8), 1183–1192.

417 (5) Xiong, B.; Zhou, R.; Hao, J.; Jia, Y.; He, Y.; Yeung, E. S. Highly Sensitive Sulphide
418 Mapping in Live Cells by Kinetic Spectral Analysis of Single Au-Ag Core-Shell Nanoparticles.
419 *Nat. Commun.* **2013**, *4* (1), 1708.

420 (6) Tang, S.; Qi, T.; Xia, D.; Xu, M.; Xu, M.; Zhu, A.; Shen, W.; Lee, H. K. Smartphone
421 Nanocolorimetric Determination of Hydrogen Sulfide in Biosamples after Silver-Gold Core-Shell
422 Nanoprism-Based Headspace Single-Drop Microextraction. *Anal. Chem.* **2019**, *91* (9), 5888–5895.

423 (7) Hang, Y.; Wang, A.; Wu, N. Plasmonic Silver and Gold Nanoparticles: Shape- and
424 Structure-Modulated Plasmonic Functionality for Point-of-Caring Sensing, Bio-Imaging and
425 Medical Therapy. *Chem. Soc. Rev.* **2024**, *53*, 2932–2971.

(8) Zhang, X.; Fu, Q.; Duan, H.; Song, J.; Yang, H. Janus Nanoparticles: From Fabrication to (Bio)Applications. *ACS Nano* **2021**, *15* (4), 6147–6191.

(9) Song, J.; Lin, L.; Yang, Z.; Zhu, R.; Zhou, Z.; Li, Z. W.; Wang, F.; Chen, J.; Yang, H.; Chen, X. Self-Assembled Responsive Bilayered Vesicles with Adjustable Oxidative Stress for Enhanced Cancer Imaging and Therapy. *J. Am. Chem. Soc.* **2020**, *141* (20), 8158–8170.

(10) Wang, X.; Huang, S. C.; Hu, S.; Yan, S.; Ren, B. Fundamental Understanding and Applications of Plasmon-Enhanced Raman Spectroscopy. *Nat. Rev. Phys.* **2020**, *2* (5), 253–271.

(11) Scarabelli, L.; Sun, M.; Zhuo, X.; Yoo, S.; Millstone, J. E.; Jones, M. R.; Liz-Marzán, L. M. Plate-Like Colloidal Metal Nanoparticles. *Chem. Rev.* **2023**, *123* (7), 3493–3542.

(12) Zhou, M.; Li, C.; Fang, J. Noble-Metal Based Random Alloy and Intermetallic Nanocrystals: Syntheses and Applications. *Chem. Rev.* **2021**, *121* (2), 736–795.

(13) Jiang, N.; Zhuo, X.; Wang, J. Active Plasmonics: Principles, Structures, and Applications. *Chem. Rev.* **2018**, *118* (6), 3054–3099.

(14) Lin, H.; Song, L.; Huang, Y.; Cheng, Q.; Yang, Y.; Guo, Z.; Su, F.; Chen, T. Macroscopic Au@PANI Core/Shell Nanoparticle Superlattice Monolayer Film with Dual-Responsive Plasmonic Switches. *ACS Appl. Mater. Interfaces* **2020**, *12* (9), 11296–11304.

(15) Yang, K.; Yao, X.; Liu, B.; Ren, B. Metallic Plasmonic Array Structures: Principles, Fabrications, Properties, and Applications. *Adv. Mater.* **2021**, *33* (50), 2007988.

(16) Suganami, Y.; Oshikiri, T.; Mitomo, H.; Sasaki, K.; Liu, Y. E.; Shi, X.; Matsuo, Y.; Ijiro, K.; Misawa, H. Spatially Uniform and Quantitative Surface-Enhanced Raman Scattering under

Modal Ultrastrong Coupling Beyond Nanostructure Homogeneity Limits. *ACS Nano* **2024**, *18* (6), 4993–5002.

(17) Gao, T.; Yachi, T.; Shi, X.; Sato, R.; Sato, C.; Yonamine, Y.; Kanie, K.; Misawa, H.; Ijiro, K.; Mitomo, H. Ultrasensitive Surface-Enhanced Raman Scattering Platform for Protein Detection via Active Delivery to Nanogaps as a Hotspot. *ACS Nano* **2024**, *18* (32), 21593–21606.

(18) Hao, J.; Xiong, B.; Cheng, X.; He, Y.; Yeung, E. S. High-Throughput Sulfide Sensing with Colorimetric Analysis of Single Au-Ag Core-Shell Nanoparticles. *Anal. Chem.* **2014**, *86* (10), 4663–4667.

(19) Szunerits, S.; Boukherroub, R. Sensing Using Localised Surface Plasmon Resonance Sensors. *Chem. Commun.* **2012**, *48* (72), 8999–9010.

(20) Sherry, L. J.; Chang, S. H.; Schatz, G. C.; Van Duyne, R. P.; Wiley, B. J.; Xia, Y. Localized Surface Plasmon Resonance Spectroscopy of Single Silver Nanocubes. *Nano Lett.* **2005**, *5* (10), 2034–2038.

(21) Zeng, J.; Li, M.; Liu, A.; Feng, F.; Zeng, T.; Duan, W.; Li, M.; Gong, M.; Wen, C.-Y.; Yin, Y. Au/AgI Dimeric Nanoparticles for Highly Selective and Sensitive Colorimetric Detection of Hydrogen Sulfide. *Adv. Funct. Mater.* **2018**, *28* (26), 1800515.

(22) Wen, X.; Bi, S.; Wang, C.; Zeng, S. An Activated Structure Transformable Ratiometric Photoacoustic Nanoprobe for Real-Time Dynamic Monitoring of H_2S in Vivo. *Nano Lett.* **2023**, *23* (22), 10642–10650.

(23) Park, G.; Lee, C.; Seo, D.; Song, H. Full-Color Tuning of Surface Plasmon Resonance by Compositional Variation of Au@Ag Core-Shell Nanocubes with Sulfides. *Langmuir* **2012**, *28* (24), 9003–9009.

(24) Mi, H.; Wang, S.; Yin, H.; Wang, L.; Mei, L.; Zhu, X.; Zhang, N.; Jiang, R. (Gold Triangular Nanoplate Core)@(Silver Shell) Nanostructures as Highly Sensitive and Selective Plasmonic Nanoprobes for Hydrogen Sulfide Detection. *Nanoscale* **2020**, *12* (39), 20250–20257.

(25) Shi, Y.; Chen, Q.; Liu, Y.; Wang, G. Capability of Au Nano-Rhombic Dodecahedra in a Label-Free Colorimetric Assay: Application in the Determination of S^{2-} and Hg^{2+}. *Analyst* **2022**, *147* (15), 3578–3584.

(26) Zhu, X.; Zhuo, X.; Li, Q.; Yang, Z.; Wang, J. Gold Nanobipyramid-Supported Silver Nanostructures with Narrow Plasmon Linewidths and Improved Chemical Stability. *Adv. Funct. Mater.* **2016**, *26* (3), 341–352.

(27) Wen, X.; Deng, S. Plasmonic Nanostructure Lattices for High-Performance Sensing. *Adv. Opt. Mater.* **2023**, *11* (16), 2300401.

(28) Ansari, J. R.; Singh, N.; Mohapatra, S.; Ahmad, R.; Saha, N. R.; Chattopadhyay, D.; Mukherjee, M.; Datta, A. Enhanced near Infrared Luminescence in Ag@Ag_2S Core-Shell Nanoparticles. *Appl. Surf. Sci.* **2019**, *463*, 573–580.

(29) Habteyes, T. G.; Dhuey, S.; Wood, E.; Gargas, D.; Cabrini, S.; Schuck, P. J.; Alivisatos, A. P.; Leone, S. R. Metallic Adhesion Layer Induced Plasmon Damping and Molecular Linker as a Nondamping Alternative. *ACS Nano* **2012**, *6* (6), 5702–5709.

(30) Jeong, H. H.; Mark, A. G.; Alarcón-Correa, M.; Kim, I.; Oswald, P.; Lee, T. C.; Fischer, P. Dispersion and Shape Engineered Plasmonic Nanosensors. *Nat. Commun.* **2016**, *7* (1), 11331.

(31) Shi, Y.; Nakamura, S.; Mitomo, H.; Yonamine, Y.; Wang, G.; Ijiro. K. Plasmonic circular dichroism-based metal ion detection using gold nanorod–DNA complexes. *Chem. Commun.* **2024**, *60* (82), 11794–11797.

(32) Zheng, G.; He, J.; Kumar, V.; Wang, S.; Pastoriza-Santos, I.; Pérez-Juste, J.; Liz-Marzán, L. M.; Wong, K. Y. Discrete Metal Nanoparticles with Plasmonic Chirality. *Chem. Soc. Rev.* **2021**, *50* (6), 3738–3754.

(33) Manoccio, M.; Esposito, M.; Primiceri, E.; Leo, A.; Tasco, V.; Cuscunà, M.; Zuev, D.; Sun, Y.; Maruccio, G.; Romano, A.; Quattrini, A.; Gigli, G.; Passaseo, A. Femtomolar Biodetection by a Compact Core-Shell 3D Chiral Metamaterial. *Nano Lett.* **2021**, *21* (14), 6179–6187.

(34) Zhou, Y.; Mazur, F.; Fan, Q.; Chandrawati, R. Synthetic Nanoprobes for Biological Hydrogen Sulfide Detection and Imaging. *View* **2022**, *3* (4), 20210008.

(35) Wang, R. Physiological Implications of Hydrogen Sulfide: A Whiff Exploration That Blossomed. *Physiol. Rev.* **2012**, *92* (2), 791–896.

(36) Zhang, Y.; Li, M.; Niu, Q.; Gao, P.; Zhang, G.; Dong, C.; Shuang, S. Gold Nanoclusters as Fluorescent Sensors for Selective and Sensitive Hydrogen Sulfide Detection. *Talanta* **2017**, *171*, 143–151.

(37) Gansel, J. K.; Thiel, M.; Rill, M. S.; Decker, M.; Bade, K.; Saile, V.; Von Freymann, G.; Linden, S.; Wegener, M. Gold Helix Photonic Metamaterial as Broadband Circular Polarizer. *Science* **2009**, *325* (5947), 1513–1515.

(38) Mark, A. G.; Gibbs, J. G.; Lee, T. C.; Fischer, P. Hybrid Nanocolloids with Programmed Three-Dimensional Shape and Material Composition. *Nat. Mater.* **2013**, *12* (9), 802–807.

(39) Kim, Y.; Yeom, B.; Arteaga, O.; Yoo, S. J.; Lee, S. G.; Kim, J. G.; Kotov, N. A. Reconfigurable Chiroptical Nanocomposites with Chirality Transfer from the Macro- to the Nanoscale. *Nat. Mater.* **2016**, *15* (4), 461–468.

(40) Probst, P. T.; Mayer, M.; Gupta, V.; Steiner, A. M.; Zhou, Z.; Auernhammer, G. K.; König, T. A. F.; Fery, A. Mechano-Tunable Chiral Metasurfaces via Colloidal Assembly. *Nat. Mater.* **2021**, *20* (7), 1024–1028.

(41) Lee, H. E.; Ahn, H. Y.; Mun, J.; Lee, Y. Y.; Kim, M.; Cho, N. H.; Chang, K.; Kim, W. S.; Rho, J.; Nam, K. T. Amino-Acid- and Peptide-Directed Synthesis of Chiral Plasmonic Gold Nanoparticles. *Nature* **2018**, *556* (7701), 360–365.

(42) González-Rubio, G.; Mosquera, J.; Kumar, V.; Pedrazo-Tardajos, A.; Llombart, P.; Solís, D. M.; Lobato, I.; Noya, E. G.; Guerrero-Martínez, A.; Taboada, J. M.; Obelleiro, F.; MacDowell, L. G.; Bals, S.; Liz-Marzán, L. M. Micelle-Directed Chiral Seeded Growth on Anisotropic Gold Nanocrystals. *Science* **2020**, *368* (6498), 1472–1477.

(43) Van Gordon, K.; Ni, B.; Girod, R.; Mychinko, M.; Bevilacqua, F.; Bals, S.; Liz-Marzán, L. M. Single Crystal and Pentatwinned Gold Nanorods Result in Chiral Nanocrystals with Reverse Handedness. *Angew. Chem., Int. Ed*. **2024**, *63*, e202403116.

(44) Wan, J.; Sun, L.; Sun, X.; Liu, C.; Yang, G.; Zhang, B.; Tao, Y.; Yang, Y.; Zhang, Q. Cu^{2+}-Dominated Chirality Transfer from Chiral Molecules to Concave Chiral Au Nanoparticles. *J. Am. Chem. Soc.* **2024**, *146* (15), 10640–10654.

(45) Ni, B.; González-Rubio, G.; Van Gordon, K.; Bals, S.; Kotov, N. A.; Liz-Marzán, L. M. Seed-Mediated Growth and Advanced Characterization of Chiral Gold Nanorods. *Adv. Mater.* **2024**, *36* (47), 2412473.

(46) Ma, Y.; Li, W.; Cho, E. C.; Li, Z.; Yu, T.; Zeng, J.; Xie, Z.; Xia, Y. Au@Ag Core-Shell Nanocubes with Finely Tuned and Well-Controlled Sizes, Shell Thicknesses, and Optical Properties. *ACS Nano* **2010**, *4* (11), 6725–6734.

(47) Atta, S.; Zhao, Y.; Sanchez, S.; Seedial, D.; Devadhasan, J. P.; Summers, A. J.; Gates-Hollingsworth, M. A.; Pflughoeft, K. J.; Gu, J.; Montgomery, D. C.; AuCoin, D. P.; Zenhausern, F.; Vo-Dinh, T. Plasmonic-Enhanced Colorimetric Lateral Flow Immunoassays Using Bimetallic Silver-Coated Gold Nanostars. *ACS Appl. Mater. Interfaces* **2024**, 16 (40), 54907–54918.

(48) Li, Y. Le; Zhu, J.; Weng, G. J.; Li, J. J.; Zhao, J. W. Controlled Spread of a Ag Layer from the Core to the Tip along the Branches of AuAg Nanostars for Improved SERS Detection of Okadaic Acid in Shellfish. *ACS Sens.* **2024**, *9* (8), 4295–4304.

(49) Lin, H.; Mitomo, H.; Yonamine, Y.; Guo, Z.; Ijiro, K. Core-Gap-Shell Nanoparticles@Polyaniline with Tunable Plasmonic Chiroptical Activities by pH and Electric Potential Dual Modulation. *Chem. Mater.* **2022**, *34* (9), 4062–4072.

(50) Mayer, K. M.; Hafner, J. H. Localized Surface Plasmon Resonance Sensors. *Chem. Rev.* **2011**, *111* (6), 3828–3857.

(51) Yip, H. K.; Zhu, X.; Zhuo, X.; Jiang, R.; Yang, Z.; Wang, J. Gold Nanobipyramid-Enhanced Hydrogen Sensing with Plasmon Red Shifts Reaching ≈140 nm at 2 vol% Hydrogen Concentration. *Adv. Opt. Mater.* **2017**, *5* (24), 1700740.

(52) Vitvitsky, V.; Kabil, O.; Banerjee, R. High Turnover Rates for Hydrogen Sulfide Allow for Rapid Regulation of Its Tissue Concentrations. *Antioxid. Redox Sign.* **2012**, *17* (1), 22–31.

(53) Xie, W.; Walkenfort, B.; Schlücker, S. Label-Free SERS Monitoring of Chemical Reactions Catalyzed by Small Gold Nanoparticles Using 3D Plasmonic Superstructures. *J. Am. Chem. Soc.* **2013**, *135* (5), 1657–1660.

(54) Ge, H.; Wang, X.; Xu, J.; Lin, H.; Zhou, H.; Hao, T.; Wu, Y.; Guo, Z. A CRISPR/Cas12a-Mediated Dual-Mode Electrochemical Biosensor for Polymerase Chain Reaction-Free Detection of Genetically Modified Soybean. *Anal. Chem.* **2021**, *93* (44), 14885–14891.

(55) Ma, X.; He, S.; Qiu, B.; Luo, F.; Guo, L.; Lin, Z. Noble Metal Nanoparticle-Based Multicolor Immunoassays: An Approach toward Visual Quantification of the Analytes with the Naked Eye. *ACS Sens.* **2019**, *4* (4), 782–791.

(56) Chen, S.; Chen, Z. J.; Ren, W.; Ai, H. W. Reaction-Based Genetically Encoded Fluorescent Hydrogen Sulfide Sensors. *J. Am. Chem. Soc.* **2012**, *134* (23), 9589–9592.

(57) Peng, H.; Cheng, Y.; Dai, C.; King, A. L.; Predmore, B. L.; Lefer, D. J.; Wang, B. A Fluorescent Probe for Fast and Quantitative Detection of Hydrogen Sulfide in Blood. *Angew. Chem., Int. Ed.* **2011**, *50* (41), 9672–9675.

(58) Qian, Y.; Karpus, J.; Kabil, O.; Zhang, S. Y.; Zhu, H. L.; Banerjee, R.; Zhao, J.; He, C. Selective Fluorescent Probes for Live-Cell Monitoring of Sulphide. *Nat. Commun.* **2011**, *2* (1), 495.

(59) Patnaik, P. Dean's Analytical Chemistry Handbook, McGraw-Hill, New York, 2nd edn, **2004**, Table 4.2, pp 1280.

(60) Zhang, N.-N.; Sun, H.-R.; Liu, S.; Xing, Y.-C.; Lu, J.; Peng, F.; Han, C.-L.; Wei, Z.; Sun, T.; Yang, B.; Liu, K. Gold Nanoparticle Enantiomers and Their Chiral-Morphology Dependence of Cellular Uptake. *CCS Chem.* **2022**, *4* (2), 660–670.

(61) Hao, T.; Zhou, H.; Gai, P.; Wang, Z.; Guo, Y.; Lin, H.; Wei, W.; Guo, Z. Deep Learning-Assisted Single-Atom Detection of Copper Ions by Combining Click Chemistry and Fast Scan Voltammetry. *Nat. Commun.* **2024**, *15* (1), 10292.

576 For Table of Contents Only

577